Electrical Pathways Through the Intricate Network of Skeletal Muscle Fibres: Insights From MRI-Validated Numerical Modeling

Rok Šmerc , Marko Stručić , Matej Kranjc , Igor Serša , Damijan Miklavčič , and Samo Mahnič-Kalamiza

Abstract-Objective: Skeletal muscles exhibit pronounced anisotropy due to their highly oriented fibre structure, a property that significantly influences the spatial distribution of tissue mechanical and electrical properties. Understanding this anisotropy is critical for advancing biomedical applications such as electrical stimulation, bioelectric impedance analysis, and novel therapeutic interventions such as pulsed field ablation (PFA). Methods: We developed a numerical model incorporating realistic skeletal muscle fibre geometry at the microscale to elucidate the origins of the experimentally observed anisotropy at the bulk tissue level. To validate the model, we evaluated the skeletal muscle anisotropy using current density imaging (CDI), a magnetic resonance-based technique. Results: The developed numerical model identifies the origins of the observed anisotropy in bulk tissue. Experimental CDI measurements validate the model, confirming that the observed current anisotropy arises from the intrinsic properties of individual muscle fibres and their organization within the tissue. Remarkably, this anisotropy persists several - even up to 48 - hours post-mortem, suggesting a structural basis that transcends the level of muscle cell membranes. Conclusion: The integration of CDI with advanced modelling provides a powerful framework for understanding and leveraging skeletal muscle anisotropy in both imaging and therapeutic applications. Significance: Our study provides an experimentally validated model of skeletal muscle that

Received 3 February 2025; revised 15 April 2025 and 16 May 2025; accepted 16 May 2025. Date of publication 22 May 2025; date of current version 14 November 2025. This work was supported by the Slovenian Research and Innovation Agency (ARIS) through the University of Ljubljana's Internal Funding for Start-up Research Programmes, Grant P2-0249 Electroporation-based technologies and treatments, Grant P1-0060 Experimental biophysics of complex systems and imaging in biomedicine, and the funding for Junior Researcher to Marko Stručić. This study was conducted within the Infrastructure Programme: Network of research infrastructure centres at the University of Ljubljana (MRIC UL IP-0510), specifically within infrastructural centre Cellular Electrical Engineering (I0-0022), also funded by the Slovenian Research and Innovation Agency (ARIS). (Rok Šmerc and Marko Stručić are co-first authors.) (Corresponding author: Samo Mahnič-Kalamiza.)

Rok Šmerc, Marko Stručić, Matej Kranjc, and Damijan Miklavčič are with the Faculty of Electrical Engineering, University of Ljubljana, Slovenia.

Igor Serša is with the Jožef Stefan Institute, Slovenia.

Samo Mahnič-Kalamiza is with the Faculty of Electrical Engineering, University of Ljubljana, 1000 Ljubljana, Slovenia (e-mail: samo.mahnic-kalamiza@fe.uni-lj.si).

This article has supplementary downloadable material available at https://doi.org/10.1109/TBME.2025.3572353, provided by the authors.

Digital Object Identifier 10.1109/TBME.2025.3572353

is relevant to biomedical applications involving electrical treatments. It also invites further experimentation using tissues immediately after harvesting, demonstrating potential use of *ex vivo* tissues as models of *in vivo* tissue, reducing the need for experimentation with live animals and the associated ethical burden.

Index Terms—Current density magnetic resonance imaging, current density distribution, ex vivo animal tissue, numerical modelling, skeletal muscle anisotropy.

I. INTRODUCTION

ANY biological tissues, such as the brain, skeletal muscle, and cardiac muscle, exhibit pronounced anisotropic properties [1], [2], [3], [4], [5], [6] that significantly influence both the current flow and the electric field distribution within them when exposed to externally applied electric fields [7], [8], [9], [10], [11]. This anisotropy arises from the structural organisation of these tissues, which leads to direction-dependent electrical and other physical properties (e.g. rates of mass and heat transfer). For example, the alignment of muscle fibres in the skeletal and cardiac muscle or the complex cellular architecture of the brain are the main causes of these anisotropic properties, which should be considered in therapeutic applications [12], [13], [14], [15], [16], [17], [18], [19].

The aforementioned tissues are often selected as target tissues in treatments involving externally applied electric fields [20], [21], [22], [23], [24]. One such example is the treatment of cardiac arrhythmias, particularly atrial fibrillation, by pulmonary vein isolation, a method commonly referred to as pulsed field ablation [25], [26], [27], [28], [29]. Another common application is gene electrotransfer, with skeletal muscle being the most common target tissue [30], [31], [32]. These therapies are based on a biophysical phenomenon called electroporation, whereby short, high-amplitude electrical pulses are delivered to biological cells or tissues, transiently permeabilising the cell membranes [33]. The increased membrane permeability facilitates the transport of ions and molecules across the membrane, thereby enabling the introduction of drugs, nucleic acids, and other molecules into the cells or their release from the cells [33], [34], [35], [36]. Depending on pulse parameters, the phenomenon can be reversible, allowing cells to survive after membrane resealing, or irreversible, causing cell death [33], with both types increasingly

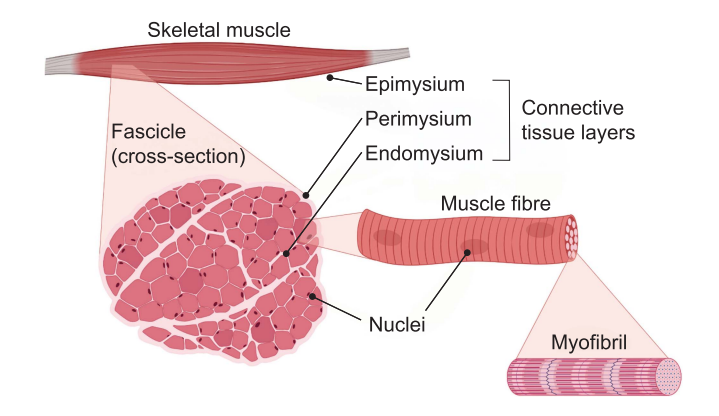


Fig. 1. The structure of skeletal muscle. The skeletal muscle is divided into various substructures, which are separated by layers of connective tissue. The entire muscle is covered by a layer of connective tissue, the epimysium. Within the muscle there are several fascicles (shown in cross-section), each of which is enveloped by the perimysium. Each fascicle consists of several muscle fibres that are enveloped by the endomysium. The muscle fibres are multinucleated and contain myofibrils. Reused from [8], licensed under CC BY 4.0.

used in biomedicine, biotechnology, and food processing [36], [37], [38], [39], [40], [41], [42]. Moreover, electrical stimulation of skeletal muscle tissue is often associated with delivery of high-voltage electrical pulses and is usually accompanied by an undesirable side effect causing pain and discomfort [43], which is therefore aimed to be minimised. Therefore, research into tissue anisotropy is crucial for optimising therapeutic procedures and outcomes. We would like to emphasise that, although this work is motivated by the relevance of anisotropic properties in tissues targeted by electroporation-based therapies, it does not directly investigate membrane permeabilisation or treatment efficacy. Instead, the study focuses on how structural anisotropy in skeletal muscle affects current density distribution during pulse application – a factor that may influence the efficacy of such procedures.

Skeletal muscle is a fibrous tissue enveloped by a layer of connective tissue, the epimysium. Within the muscle there are several fascicles with a diameter of 1–10 mm, which are separated by another layer of connective tissue, the perimysium. Each fascicle consists of several muscle fibres with a diameter of 20-100 µm, which are separated by the endomysium, the innermost layer of connective tissue (Fig. 1) [44], [45], [46], [47]. Each layer of connective tissue forms a complex structure with varying density and composition. To further increase the complexity of skeletal muscle, nerve fibres and blood vessels are closely interwoven with these layers of connective tissue [48]. Muscle fibres are polynucleated cells ranging in length from millimetres to several tens of centimetres and contain myofibrils, which consist of the contractile muscle proteins [49]. The muscle fibres are specialised to contract in response to signals from associated nerve endings called motor endplates. The fibres transmit these signals by propagating the action potential along their sarcolemma [50]. The primary carriers of electrical charge in biological tissues are ions. Their movement is restricted by insulating structures such as the sarcolemma and connective tissue layers (e.g. epi-, peri-, and

endomysium), leading to electrical anisotropy, especially at low frequencies [6], [51].

Since many biological tissues have heterogeneous structures, which can result in anisotropic properties, it is important to obtain spatial information on their electrical properties, such as conductivity distribution maps, or alternatively, the distribution of current density or electric field within the tissue when exposed to an external electric field [52]. The heterogeneous distribution of conductivity has already been observed, e.g., in tumour or brain tissue [53], [54], [55], [56]. In CDI, the magnetic field change is recorded in a phase of an MR image, which is then used to calculate the corresponding magnetic field created by the currents, and finally from these the current density using Ampere's law [57]. Since its introduction in 1989, CDI has become a versatile method for study electrical conductivity properties in DC [58], AC [59], and RF [60] frequency ranges of various biological samples [61], [62], [63] or materials [64].

In this study, we investigate the origins of electrical anisotropy in skeletal muscle using a combination of numerical modelling and experimental validation. The work follows from our previously published study [8] and continues the multiscale approach whereby the bulk properties of tissue follow from properties of individual constituents and their geometrical organisation. Although our earlier work addresses muscle anisotropy by comparing lesion sizes resulting from electric fields applied in different orientations relative to muscle fibres, such outcome-based validation remains indirect, as it does not explicitly confirm the modelled electrical behaviour arises from the geometrical organisation and biophysical properties of individual muscle fibres. To address this, we developed a three-dimensional model based on anatomically realistic muscle fibre architecture and used current density imaging (CDI), a magnetic resonance-based method, for experimental validation. The model was specifically designed to disentangle the contributions of muscle microstructure, such as fibre alignment and membrane electrical impedance, from other confounding variables. By comparing parallel and perpendicular electrode orientations in both the model and experiments, we aim to explain how skeletal muscle structure alone governs current flow and anisotropic behaviour within tissue. This approach offers new insights into tissue-scale electrical properties, with implications for electrical therapies, bioimpedance measurements, and treatments or diagnostics based thereon.

II. MATERIALS AND METHODS

A. Numerical Computations

The numerical model was built and solved with the COMSOL Multiphysics software environment (version 6.2, COMSOL AB, Stockholm, Sweden) using the finite element method. A three-dimensional geometry was used to approximate the experimental muscle tissue sample, with slightly reduced dimensions to increase computational efficiency of the simulations. The tissue was modelled as a cylinder with a diameter of 20 mm and a height of 0.5 mm, whereas the muscle fibres were represented as cylinders with a diameter of 60 μ m spanning the entire domain. The geometry was designed so that the volume fraction of the muscle fibres was 78 %, which falls within the range typically

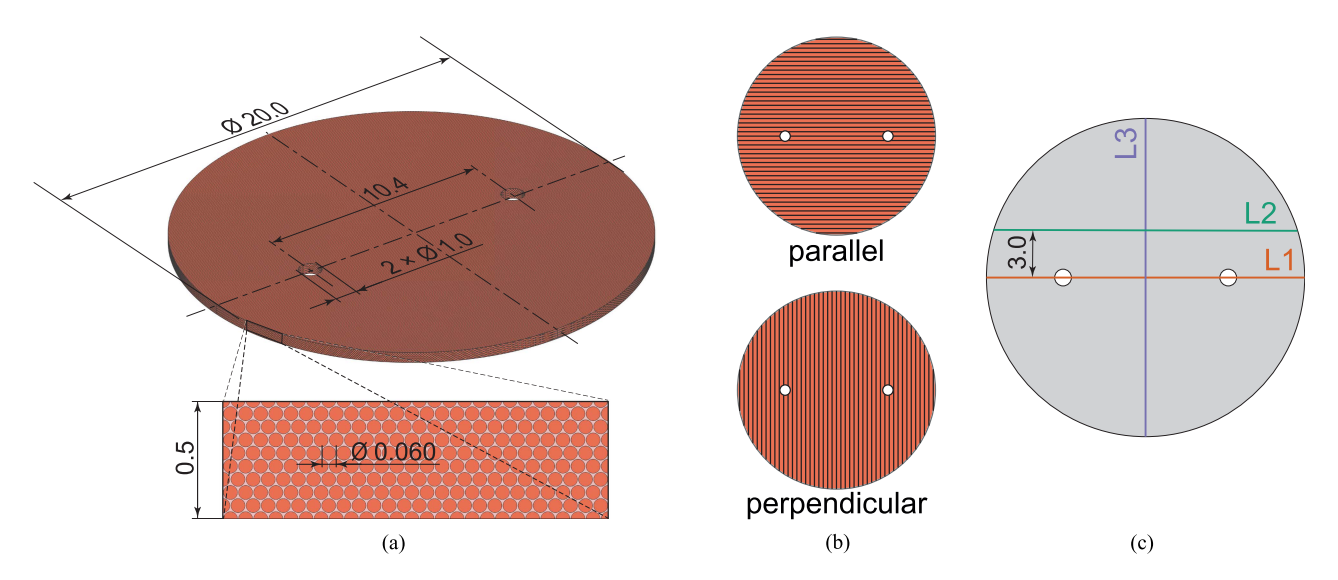


Fig. 2. (a) Geometry and dimensions of the muscle tissue sample as modelled in COMSOL Multiphysics. Note that all dimensions are in mm. (b) The two orientations of the inserted electrodes relative to the orientation of the muscle fibres: in the parallel orientation, the electrodes are positioned so that the direction of the applied electric field is parallel to the muscle fibres; in the perpendicular orientation, the field is perpendicular to the fibre orientation. (c) The three lines (L1, L2, L3) selected for detailed analysis of the current density distribution in both the numerical simulations and the experimental measurements.

reported in the literature for the muscle tissue [65]. The plasma membranes, whose thickness is several orders of magnitude smaller than that of the other dimensions, were not included explicitly but were instead modelled using a Contact Impedance boundary condition. Specifically, the contact impedance values were derived from the ratio of the membranes' thickness to their conductivity, effectively capturing the essential resistive effect of the membranes while avoiding the computational expense of resolving the submicrometre geometry. This ensures that the contribution of the membranes to the current flow is preserved without significantly increasing the complexity of the finite element mesh. The geometry, including all dimensions, is shown in Fig. 2(a). The electrodes were inserted into the tissue in two different orientations relative to the muscle fibre alignment (see Fig. 2(b)). In the parallel orientation, the electrodes were positioned so that the direction of the applied electric field was parallel to the muscle fibres. In perpendicular orientation, the electric field was perpendicular to the fibre orientation. The model was solved using the Electric Currents physics interface with a stationary study. This approach was appropriate because the CDI technique captures the cumulative effect of the electric current on the MR signal phase and thus represents the timeaveraged current density over the duration of the applied pulse. Therefore, a stationary study provides a suitable approximation of the experimentally observed behaviour. A voltage of 100 V was applied, matching the amplitude used in the experimental setup. The model was discretised with approximately 19.5 million finite elements. The primary goal of the simulation was to calculate the current density distribution, represented as a vector field, for both the parallel and perpendicular orientations. The current density distribution was then analysed in more detail along three specific lines L1, L2, and L3 (see Fig. 2(c)). The current density at each specific line was normalised by the maximum value of the current densities from both the parallel

TABLE I
PARAMETERS AND THEIR CORRESPONDING VALUES USED IN THE
NUMERICAL MODEL [65], [66], [67]

Parameter	Value	Description
f	0.78	Volume fraction of fibres
$\sigma_{ m i}$	0.55 S/m	Intracellular conductivity
$\sigma_{ m e}$	1.20 S/m	Extracellular conductivity
$\sigma_{ m m}$	2.5×10^{-5} S/m	Membrane conductivity
$t_{ m m}$	7 nm	Membrane thickness

and perpendicular orientations for that particular line, ensuring the ratio between the two orientations was maintained. The parameters and their corresponding values used in the model are listed in Table I. Note that the conductivity of the cell plasma membranes was adjusted by approximately two orders of magnitude from typical values found in literature to account for the at least partial disintegration of the membranes within 48 hours from the muscle tissue extraction. This is due to the experiments being performed *ex vivo*, 48 hours *post-mortem*, in which time the skeletal muscle membranes are expected to undergo a certain degree of (gradual) disintegration. The post-processing of the simulation results was performed using Python.

B. Experimental Study

Samples of porcine muscle tissue were acquired 2 hours *post-mortem* from the biceps femoris and trapezius muscles. We chose muscles with a uniform alignment of fibres to be able to ensure consistency in the orientation of the applied electric field, whether parallel or perpendicular to the fibres. The tissue was obtained from a slaughterhouse that operates in accordance with Slovenian law. Sections measuring $10 \text{ cm} \times 10 \text{ cm} \times 10 \text{ cm}$ were excised from both sites, cooled to $4 \, ^{\circ}\text{C}$ and stored for

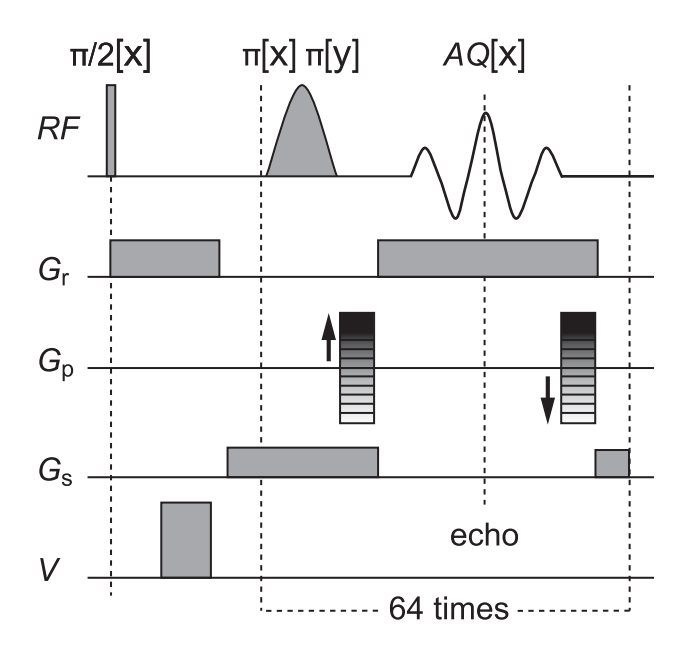


Fig. 3. Two-shot RARE pulse sequence for monitoring the current density distribution during external electrical pulse delivery. The sequence begins with a non-selective 90° radiofrequency (RF) excitation pulse, immediately followed by the current encoding part with an $800~\mu s$, 100~V electrical pulse (V). Signal acquisition is then performed using the single-shot RARE scheme with readout (G_r) , phase-encoding (G_p) , and slice-selection (G_s) magnetic field gradients. Due to the phase shifts induced by the electrical pulse, the sequence is repeated twice, first with refocussing pulses of phase 0° and then of phase 90° with respect to the phase of the excitation pulse, and the corresponding two acquired signals are co-added [69].

48 hours for transport to the experimental facility. Smaller cylindrical samples (20 mm in height and 26 mm in diameter) were then cut from these sections to fit into a custom-made acrylic glass container for MRI analysis. The samples were cut so that the muscle fibres were aligned perpendicular to the axis of the cylinder and no visible fascia was present. Prior to the experiments, the tissue samples were allowed to warm up to room temperature. The samples were divided into two groups based on the orientation of the applied electric field. In the parallel orientation, the direction of the applied field was parallel to the muscle fibres, whereas in the perpendicular orientation it was perpendicular to the fibres (Fig. 2(b)). For each of the two orientations, three samples were prepared from each of the biceps femoris and trapezius muscles, resulting in a total of twelve samples. Two platinum-iridium alloy (90:10 w%) needle electrodes with a diameter of 1 mm were inserted into the centre of the sample, with a centre-to-centre distance of 10.4 mm. A single short electrical pulse with an amplitude of 100 V and a duration of 800 µs was delivered between the electrodes using a laboratory prototype pulse generator (University of Ljubljana, Ljubljana, Slovenia), based on an H-bridge digital amplifier with 1 kV MOSFETs (DE275-102N06 A, IXYS, Milpitas, CA,

A two-shot rapid acquisition with relaxation enhancement (RARE) pulse sequence imaging was used to perform the CDI (Fig. 3). Each sequence contained the aforementioned 800 µs, 100 V electrical pulse, delivered immediately after the initial

 $\pi/2$ radiofrequency (RF) pulse [69], [70]. Data acquisition was performed using an NMR/MRI system (Tecmag, Houston, TX, USA) connected to a 2.35 T horizontal bore superconducting magnet (100 MHz proton MR frequency, Oxford Instruments, Abingdon, U.K.). The system was equipped with gradient hardware capable of delivering maximum gradient pulses of 250 mT/m (Bruker, Ettlingen, Germany). The spectrometer featured programmable TTL outputs for controlling peripheral devices, one of which triggered the external electrical pulses on the pulse generator and synchronised them with the imaging sequence. The imaging parameters included a 30 mm field of view, a 64 x 64 imaging matrix, an inter-echo delay of 2.64 ms, a RARE factor of 64 and an echo time of 20 ms.

The lower sensitivity limit of CDI is inversely proportional to the presence of noise in the phase image, whereas the upper sensitivity limit depends on the product of the delivered current (I) and the total duration of the applied electric pulses (t_c) . Since the phase signal-to-noise ratio (SNR) is not significantly affected by the application of electrical pulses, the sensitivity of the CDI can only be improved by increasing the amplitude or duration of these pulses. To increase CDI sensitivity and enable current density detection at lower current levels, we extended the pulse duration to 800 µs. However, further increasing the pulse duration beyond this point would have a negative effect on the overall SNR. This is because in spin-echo-based imaging sequences, the MR signal decays exponentially with time due to T_2 relaxation, following the relationship SNR $\propto \exp(-T_{\rm E}/T_2)$, where $T_{\rm E}$ is the echo time. A longer pulse duration would increase the $T_{\rm E}$ and thus reduce the signal strength and therefore the lower sensitivity limit of the CDI.

One might note the substantial difference between the Larmor frequency ($\sim 100 \text{ MHz}$ at 2.35 T) and the lower characteristic frequency ($\sim 1.25 \text{ kHz}$) of an 800 μs pulse. However, electric pulses induce a phase shift in the NMR signal that is proportional to the time integral of the applied current. This phase shift is retained throughout the imaging sequence and appears in the phase of the resulting MR image. Importantly, the CDI technique captures the cumulative effect of the electrical current on the phase of the MR signal, i.e. it reflects the time-averaged current density over the duration of the pulse. As such, CDI is independent of the Larmor frequency or the frequency content of the applied pulses and depends only on the pulse duration and amplitude.

After data acquisition, the imaged slices were reconstructed using ImageJ (version 1.53, National Institutes of Health, Bethesda, MD, USA). The slices were then realigned to standardise the electrode positions and ensure consistent alignment to facilitate comparison between slices during post-processing. Following reconstruction and alignment, the images were imported into MATLAB (version R2024a, MathWorks Inc., Natick, MA, USA) to reconstruct the current density vector fields. The samples were divided into two groups: one in which the electrodes were positioned so that the direction of the applied electric field was parallel to the muscle fibres, and the other in which the field was perpendicular to the fibre orientation. No distinction was made between the biceps femoris and trapezius muscle samples, as both are skeletal muscles that show no

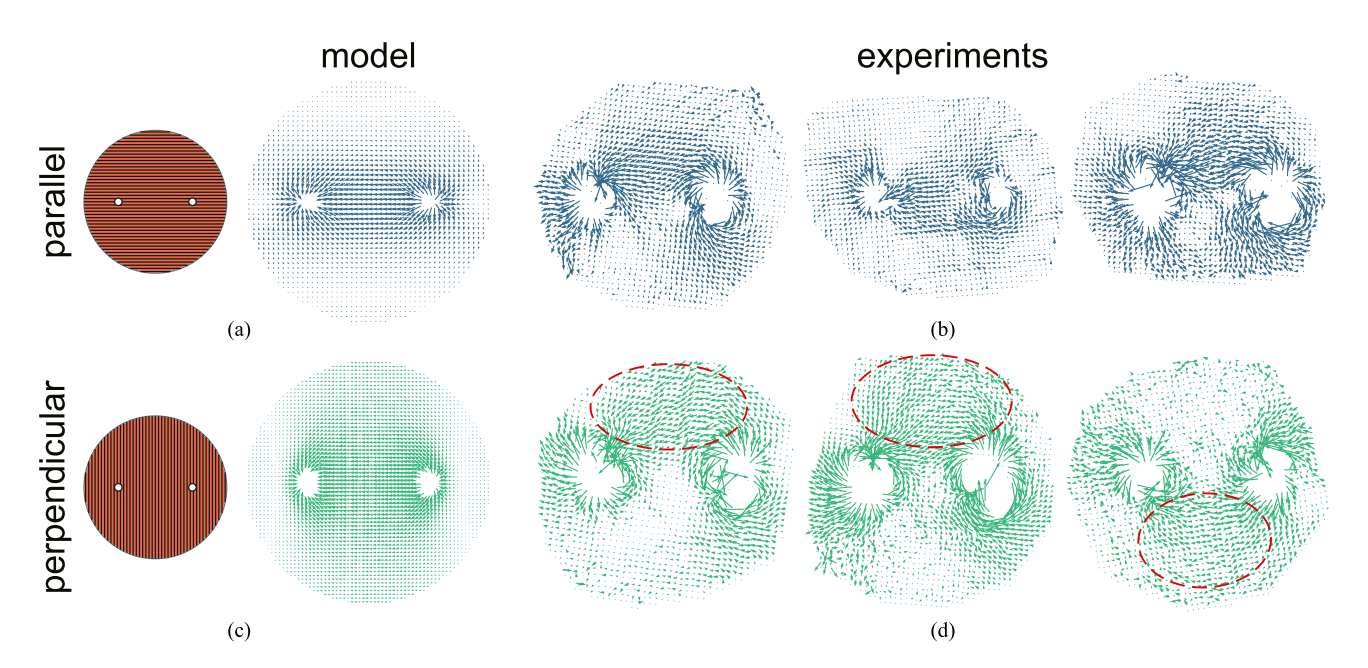


Fig. 4. Vector fields (amplitude and direction) representing the current density distribution in the muscle tissue samples. The simulation results are presented in (a) and (c), and the experimental results, representing three exemplary replicates out of six from each orientation in (b) and (d). In (a) and (b) the electrode orientation was parallel (i.e., the electric field was applied in a direction parallel with respect to the direction of the muscle fibres) and in (c) and (d) it was perpendicular (i.e., the electric field was applied in a direction parallel with respect to the direction of the muscle fibres). Red dashed ellipses show the displacement of the current away from the central area between the electrodes, as the current flow is deflected in the direction of the muscle fibres.

marked differences in properties. The current density data for all samples were then determined along the three specified lines L1, L2, and L3, as shown in Fig. 2(c), and each subsequently normalised by the maximum current density value from each individual experiment (twelve samples in total, six for each orientation). For each line, the set of voxels nearest to the defined path was selected for analysis, with the width of the line corresponding to a single voxel to ensure that no information was lost by averaging across multiple voxels.

C. Statistical Methods

No statistical tests were carried out for the numerical results, as each simulation result is deterministic and consistently reproducible under identical conditions.

For the experimental results, vector fields were presented for each electrode orientation (parallel and perpendicular). These were not averaged to preserve the details of the fields and avoid potential loss of information. In the analysis of current density along the three selected lines (L1, L2, and L3; Fig. 2(c)), the data from six samples in each orientation group (parallel and perpendicular) were averaged across each location along the lines L1, L2, and L3, with the results presented as mean values with standard deviations to illustrate the variability within each group.

To assess the statistical differences between the parallel and perpendicular orientations, data at each spatial coordinate (position) along the observation lines were first tested for normality using the Shapiro-Wilk test, and for homogeneity of variances using the Brown-Forsythe test. Because unequal variances were

observed at some positions, Welch's t-test (two-tailed, unpaired, and not assuming equal variances) was performed at each position. In addition, a false discovery rate (FDR) correction using the Benjamini-Hochberg method was applied to control false positives. The resulting p-values were used to identify segments where statistically significant differences (p < 0.05) occurred. The electrode regions along line L1 were excluded from the statistical tests.

III. RESULTS

The result of current density imaging (CDI) is a vector field in a slice of three-dimensional tissue that ascribes a vector of electric current with its amplitude and direction to each voxel. The most common method of visualising this vector field is given in Fig. 4. This method allows visualising the areas of highest current density but is not the most suitable for performing quantitative comparison and analysis. To the latter, an analysis of only the amplitude of the current density vector is more suited, but since we thereby lose the directionality information, we analysed the amplitude only along selected dissection planes/lines as defined in Fig. 5.

Fig. 4 shows the current density distribution in the muscle tissue samples, represented as vector fields. Both simulation results (Fig. 4(a) and (c)) and experimental results (Fig. 4(b) and (d)) are shown, comparing parallel (Fig. 4(a) and (b)) and perpendicular (Fig. 4(c) and (d)) orientations. For the experimental data, three exemplary replicates out of six are shown for each orientation. No distinction was made between the biceps femoris and trapezius muscle samples, as both are skeletal muscles that

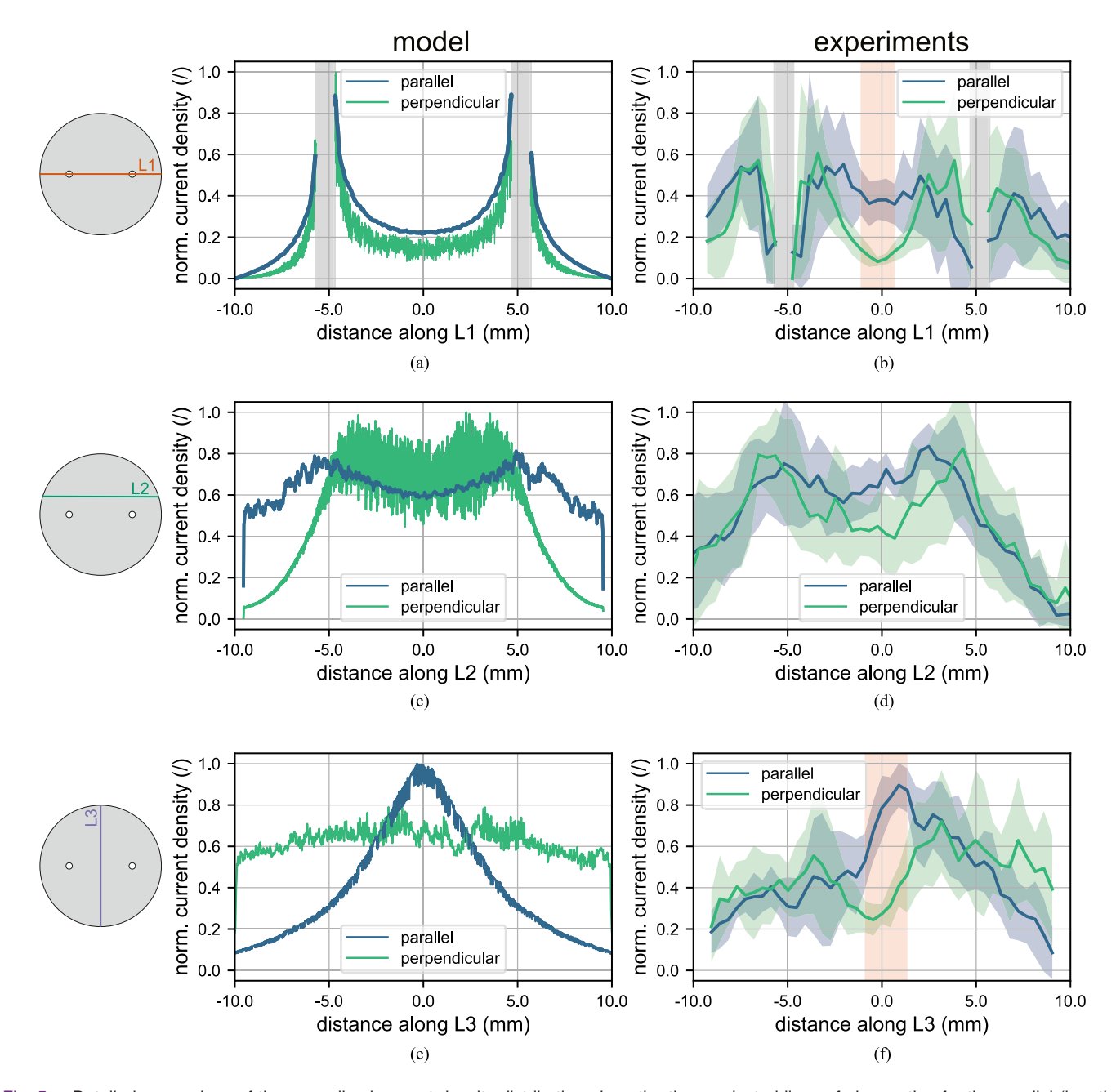


Fig. 5. Detailed comparison of the normalised current density distribution along the three selected lines of observation for the parallel (i.e., the electric field was applied in a direction parallel with respect to the direction of the muscle fibres) and perpendicular (i.e., the electric field was applied in a direction parallel with respect to the direction of the muscle fibres) groups. The results along the line L1 are shown in (a) and (b), along the line L2 in (c) and (d), and along the line L3 in (e) and (f). The simulation results are shown in (a), (c), and (e), whereas the experimental results are shown in (b), (d), and (f). In (a) and (b), the grey shaded regions indicate the position of the electrodes. In (b), (d), and (f), the results are given as mean values \pm standard deviations (shaded areas), with N=6. The red shaded regions in (b) and (f) indicate segments along the observation lines where a statistically significant difference (p<0.05) was observed between the parallel and perpendicular groups.

exhibit no marked differences in properties. In the simulation results for the parallel orientation (Fig. 4(a), the current flows predominantly along the shortest path between the electrodes. In contrast, for the perpendicular orientation (Fig. 4(c)), the current is more evenly distributed across the tissue section with no clear preferred path, indicating a less preferential flow. The experimental results show similar behaviour. In the parallel orientation (Fig. 4(b)), most of the current flows predominantly along the shortest path between the electrodes, consistent with the

simulations. However, in the perpendicular orientation (Fig. 4(d)), the current flow is deflected in the direction of the muscle fibres rather than favouring the shortest path, similar to the modelling results (Fig. 4(c)). A corresponding visualisation of the spatial distribution of normalised current density amplitude is provided in the Supplementary Materials (Fig. S1).

The normalised current density distribution along three selected lines (L1, L2, and L3) for the parallel and perpendicular electrode orientation is compared in Fig. 5. Both simulation

(Fig. 5(a), (c), and (e)) and experimental (Fig. 5(b), (d), and (f)) data are shown. For the experimental data, twelve samples (six for each orientation, including both biceps femoris and trapezius muscle samples) were analysed and compared. No distinction was made between the biceps femoris and trapezius muscle samples, as both are skeletal muscles that exhibit no marked differences in properties. An alternative version of Fig. 5 is included in the Supplementary Materials as Fig. S2, showing the same mean values, but with shaded regions representing the full range (minimum to maximum) across samples instead of standard deviations.

For line L1, the simulation results (Fig. 5(a)) show that the current density between the electrodes is higher in the parallel orientation than in the perpendicular orientation, indicating that current flows preferentially along the shortest path between the electrodes. The experimental results confirm this observation. The statistical analysis revealed a significant difference (p < 0.05) between the two orientations in a 1.8 mm wide region at the centre of the observation line (Fig. 5(b)).

For line L2, the simulation results (Fig. 5(c)) indicate that the current density is more evenly distributed along the line in the parallel orientation, with a slightly lower amplitude compared to the perpendicular orientation. The experimental results (Fig. 5(d)) show similar distribution but no statistically significant differences between the parallel and perpendicular orientations.

For line L3, the simulation results (Fig. 5(e)) show a pronounced peak in current density at the centre of the line in the parallel orientation, again suggesting that the current flows preferentially along the shortest path between the electrodes. In contrast, in the perpendicular orientation, the current is more evenly distributed along the entire line. The experimental results (Fig. 5(f)) show a similar trend for the parallel orientation, with a pronounced peak in the centre of the line. However, for the perpendicular orientation, the experimental results show that the current is deflected in the direction of the muscle fibres, either above or below the line connecting the electrodes, resulting in a minimum of current density in the mid-line region. Because this deflection varies from sample to sample, shifting above the electrode axis in some cases and below in others, averaging the results of all six experiments leads to an artificial appearance with two peaks and a dip in the centre. This is not due to two distinct current paths, but rather the result of averaging variable deflection patterns. The statistical analysis revealed a significant difference (p < 0.05) between the two orientations in a 2.3 mm wide region at the centre of the observation line.

IV. DISCUSSION

The present study follows from our previously published work [8]. The multiscale numerical model described therein models tissue anisotropy by accounting for membrane permeabilisation of individual constituent cells that are represented as heavily elongated cuboidal cells [71], [72], [73]. Elongated as they may be, these individual cells modelled in the multiscale model of a skeletal muscle are still far from being true to the anatomical structure of an actual muscle fibre extending from

several millimetres to tens of centimetres in length. In the newly developed model, the skeletal muscle tissue comprises many thin cylinders representing individual muscle fibres of realistic dimensions. We thus remain true to the adage of building a model from the ground up (i.e., a multiscale numerical model) whilst observing behaviour and properties on the macro scale (i.e., in bulk tissue). Due to the increased anatomical complexity of the model, particularly the inclusion of individual muscle fibres in the bulk tissue, it was necessary to reduce the numerical complexity to ensure computational feasibility. To achieve this, we employed a static approach rather than a dynamic time-domain simulation. Furthermore, we opted not to account for the changes in electrical material properties that may occur in the tissue due to membrane permeabilisation. However, these decisions should not be considered as limitations, as the primary aim of our work was to investigate the intrinsic anisotropy of skeletal muscle tissue, in particular its initial properties before such changes would occur. We wish to emphasise that the specific experimental parameters used in this study (i.e., a single 800 µs pulse at 100 V, resulting in the maximum theoretical 100 V/cm voltageto-distance ratio as an estimate of the peak electric field strength) were selected to remain below the established electroporation thresholds for skeletal muscle tissue under similar conditions. Due to electrode geometry (needle electrodes), most of the tissue experienced well under 100 V/cm, since our intent was to study the intrinsic anisotropy of the tissue without significantly altering its structure or electrical properties due to membrane permeabilisation. In our case, the tissue used was ex vivo and 48 hours *post-mortem*, meaning cell membranes were already partially disintegrated. This likely diminished the contribution of active membrane resistance to overall anisotropy, shifting the observed anisotropic behaviour more toward structural and extracellular matrix properties (e.g., alignment of collagenous structures). We therefore expect that any membrane permeabilisation effects at these low field strengths had minimal additional influence on the observed anisotropy.

To experimentally validate the model, we performed current density imaging (CDI) experiments on *ex vivo* porcine muscle tissue. An electric pulse was delivered to observe the current flow in tissue. We positioned the electrodes in two specific orientations: one in which the applied electric field was parallel to the muscle fibres and one in which it was perpendicular to them. This arrangement allowed a comprehensive investigation of the anisotropic properties of the tissue. The purpose of this was to explore the anisotropy through advanced numerical modelling and to experimentally validate the model's predictions visualising the current flow within the tissue by means of CDI.

Main results of our study are current density distributions for the experimentally obtained data on muscle tissue and their counterparts obtained via numerical modelling. Both were analysed for the case of parallel and perpendicular direction between the electric field and main axis of the muscle fibres. The model was constructed following our previous work [8] with the aim of providing a theoretical background and offer a possible mechanism for the observed anisotropy, and the experimental part of the study validates the premises on which the model

is built through a good correlation between vector fields and amplitudes in current density obtained in both ways.

The results underline the anisotropic behaviour of muscle tissue under electric fields, which is evident both in the modelling and in the experimental data. The deflection of the current flow in the perpendicular orientation (Fig. 4(d)) is likely caused by the resistance posed by tissue structures with a much lower electrical conductivity than the intra- and extracellular conductivities, such as sarcolemma or connective tissue layers, at the level of the muscle fibres. These structures impede the flow of current in directions perpendicular to the longitudinal axis of the fibres. An alternative view of this behaviour, highlighting, for example, the difference between the first sample in Fig. 4(b) and the last in Fig. 4(d), is provided in the Supplementary Materials (Fig. S1), which displays the spatial distribution of current density amplitude across all samples. In contrast to the perfectly symmetrical flow patterns observed in the model, the experimental results show asymmetries in the current flow. These discrepancies likely arise from inherent tissue heterogeneities, such as local variations in the density of muscle fibres or composition of connective and adipose tissue, or other structural components (e.g. vessels, capillaries, nerves). Such heterogeneities create pathways with different resistances, influencing the preferential current flow observed in the experiments. The keen reader will have noticed a strong apparent divergence of the current field at both electrodes in the experimental results, occurring at the anode as well as the cathode. The direction of the current vectors near the electrodes at the electrode-tissue boundary and between the electrodes and the edge of the tissue shows inconsistent behaviour, which is an artefact of the CDI reconstruction algorithm that has problems with reconstructing the direction of current at the electrodetissue interface, and which we were not able to fully mitigate in post-processing. Please note that the directionality (but not the amplitude, which remains unaffected) of the vector fields in these boundary regions is not reliable.

The results from Fig. 5 confirm the findings on the anisotropic behaviour of muscle tissue observed in Fig. 4 and allow quantitative comparison of results obtained by modelling and by CDI. In the parallel orientation, both the simulations and the experimental results consistently show a higher current density along the shortest path in the region between the electrodes. This supports the idea that the current flows preferentially along this path due to the muscle tissue structure, i.e., fibre composition and orientation. The lack of apparent differences in the experimental results for line L2 could be due to *post-mortem* changes in the tissue, as we used ex vivo tissue samples 48 hours post-mortem. These changes may have affected the tissue properties so that the differences between the parallel and perpendicular orientations were less pronounced. Changes such as membrane disintegration may have affected the observed results, resulting in no clear differences between the orientations. To support this hypothesis, we note that electrical impedance measurements (as of yet unpublished, preliminary experimental data obtained in a separate, conceptually related study) performed on similar muscle tissue at different post-mortem time points (3 h, 24 h, and 72 h) showed a clear decline in anisotropy over time. These results suggest that structural degradation, particularly of cell membranes, can

diminish the degree of tissue anisotropy. A potential avenue for future work would be to repeat the CDI measurements on fresher tissue or across multiple *post-mortem* intervals to directly correlate anisotropy loss with time-dependent microstructural changes.

The deflection of current flow in the perpendicular orientation observed in the experimental results, particularly in line L3, again suggests that tissue heterogeneity plays a role in controlling current flow. In contrast to the symmetrical flow patterns observed in the simulations, the experimental results seem to exhibit a preferential current path that deviates from the shortest path between the two electrodes. We propose that the observed pattern likely results from the formation of preferential current paths during the experiment, which emerge from minute, spatially varying differences in tissue conductivity; for example, due to slight differences in hydration, fibre alignment, or local membrane degradation. Such heterogeneities can seed current redistribution, where slightly more conductive regions near one electrode facilitate higher current densities early on in a particular direction at a non-zero (and possibly substantial) angle with respect to the shortest path between the two electrodes. Once this preferential path is established, the non-linear dependence of conductivity on field strength may reinforce this route as the current continues to flow, effectively amplifying the initial asymmetry into a consistent directional pattern. We have observed something quite similar very early on in our MRI-based experiments, on agarose phantoms [74].

The experimental results indicate that the skeletal muscle tissue exhibits anisotropy even days after excision. This suggests that the observed anisotropic properties are not solely a function of the plasma membrane of living cells but may also be attributed to the collagenous composition of the muscle structures. This inherent anisotropy could be due to the orientation and structure of collagen and other extracellular matrix components, but also intracellular structures such as actin and myosin in the sarcomere (as the membrane is already disintegrated), that contribute to the overall resistance to current flow in muscle tissue. These structural components remain in the tissue after death and form the basis for the anisotropic behaviour, even after the disintegration of the cell membranes. We should at this point clarify that while our computational model assumes that muscle tissue anisotropy arises predominantly from the relative conductivities of the intracellular and extracellular spaces and the resistive effect of the cell membrane, the experimental data were acquired from ex vivo tissue 48 hours post-mortem. By this time, the structural and functional integrity of the plasma membranes is likely compromised to a significant extent. As such, the experimentally observed anisotropy is probably governed less by the membrane resistance and more by the properties and spatial organisation of the extracellular matrix and remaining intracellular architecture. This implies that although the model parameters (e.g., membrane conductivity, intracellular and extracellular conductivity) provide a computationally robust framework for simulating anisotropic current flow, they may not fully correspond to the mechanistic properties governing anisotropy under the experimental conditions. Nevertheless, the consistency between simulated and experimental data indicates

that the model remains valuable for probing the structural determinants of tissue anisotropy, even if the biophysical meaning of certain parameters must be interpreted with caution in the context of *post-mortem* tissue.

To evaluate the robustness of the experimental results, we investigated the influence of line positioning (particularly the line L2) and the selected width (i.e., the number of voxels) of the lines L1, L2, and L3 on the current density distributions. The position of line L2 had no significant influence on the results when its distance from line L1 varied slightly (within \pm 1 mm). However, when L2 was moved closer to L1 (to within 1 mm), the amplitude of the parallel current density became higher than that of the perpendicular orientation. Conversely, the perpendicular current density increased relative to the parallel orientation when L2 was moved further away from L1 towards the edge of the sample.

If the width of the lines was increased to three voxels, this had no significant effect on the results, except for minor local deviations at certain points. We chose to use a line width of a single voxel, in order to avoid the potential loss of detail that could result from averaging across a larger width, which could blur spatial variations and reduce the accuracy of the current density distribution along the lines. We believe this approach ensures that the results reflect the actual variations in current density with minimal smoothing or distortion, thereby providing a more accurate representation of the anisotropic properties of the tissue.

It is also important to consider other factors that could influence the results of the model. One of these is the role of muscle fibre volume fraction and the possible effects of membrane permeabilisation near the electrodes. In our previous work [8], we have already investigated the influence of muscle fibre volume fraction on the anisotropy rate in skeletal muscle tissue. As described in the Supplementary Material of [8], the influence of volume fraction on the anisotropy rate was found to be negligible, although it affected the absolute values of conductivity in the parallel and perpendicular orientations. This indicates that the results of the current model are not significantly dependent on the volume fraction of the muscle fibres.

Factors such as variations in muscle fibre density and orientation, as well as the presence of different tissue types, including connective and adipose tissue, vessels, capillaries, and nerves, could influence electrical properties and current flow. These factors are not explicitly accounted for in the model, which could have led to the observed discrepancies between the model's predictions and experimental results. Furthermore, the model assumes a uniform tissue geometry. Although this simplifies the representation of muscle tissue, it cannot fully capture the natural heterogeneity that exists *in vivo*.

Despite providing valuable insights into the anisotropic behaviour of muscle tissue, certain limitations must be considered when interpreting the results. The first limitation is that the experiments were performed 48 hours *post-mortem*. By this time, the plasma membranes have at least partially disintegrated. This means that the tissue does not show the same behaviour as fresh tissue, which may limit the transferability of the results to *in vivo* conditions.

Another potential limitation is the possibility of the alteration of tissue electrical properties due to permeabilisation of membranes near the electrodes. In our study, we used a single pulse of 800 µs duration and a low amplitude of 100 V, which should not induce significant changes except possibly in the immediate vicinity of the electrodes. Although it may be beneficial to include membrane permeabilisation in the model to account for potential changes in the electrical properties of the tissue, as has been done previously [8], [71], [72], [73], this would significantly increase the computational complexity of the simulations. Given the state of the tissue under the experimental conditions (disintegrated membranes at 48 hours *post-mortem*), such effects are expected to have minimal impact on the results.

V. CONCLUSION

In conclusion, our study presents three key contributions to understanding skeletal muscle tissue and its material properties.

Firstly, our geometrically complex yet simplified model, with minimal degrees of freedom in material properties, illustrates how muscle anisotropy arises from the muscles' structure. The model serves as a strong foundation for further development, including incorporating living (*in vivo*) cell membranes whose permeability and conductivity could be modelled as treatment-dependent.

Secondly, our findings confirm that muscle tissue anisotropy can be effectively studied via electric current using state-of-theart magnetic resonance imaging methods, such as CDI. While the necessary equipment is available only to select research groups, established methods in the literature provide a pathway for further experimentation provided the necessary equipment is acquired.

Thirdly, our results suggest that skeletal muscle tissue retains a detectable degree of anisotropy even days post-excision, indicating that this property may not be solely dependent on the plasma membrane of living cells but also (in part, at least) on the collagenous composition and internal structures like actinand myosin-containing sarcomeres.

These promising experimental results encourage further studies on freshly harvested tissues (minutes to a couple of hours *post-mortem*) to explore the plasma membrane's role in bulk anisotropy.

REFERENCES

- B. R. Epstein and K. R. Foster, "Anisotropy in the dielectric properties of skeletal muscle," *Med. Biol. Eng. Comput.*, vol. 21, no. 1, pp. 51–55, Jan. 1983.
- [2] K. R. Foster and H. P. Schwan, "Dielectric properties of tissues and biological materials: A critical review," *Crit. Rev. Biomed. Eng.*, vol. 17, no. 1, pp. 25–104, 1989.
- [3] C. Gabriel, S. Gabriel, and E. Corthout, "The dielectric properties of biological tissues: I. Literature survey," *Phys. Med. Biol.*, vol. 41, no. 11, pp. 2231–2249, Nov. 1996.
- [4] S. Gabriel, R. W. Lau, and C. Gabriel, "The dielectric properties of biological tissues: II. Measurements in the frequency range 10 hz to 20 GHz," *Phys. Med. Biol.*, vol. 41, no. 11, pp. 2251–2269, Nov. 1996.
- [5] S. Gabriel, R. W. Lau, and C. Gabriel, "The dielectric properties of biological tissues: III. Parametric models for the dielectric spectrum of tissues," *Phys. Med. Biol.*, vol. 41, no. 11, pp. 2271–2293, Nov. 1996.

- [6] D. Miklavčič, N. Pavšelj, and F. X. Hart, "Electric properties of tissues," in Wiley Encyclopedia of Biomedical Engineering, 1st ed., M. Akay, Ed. Hoboken, NJ, USA: Wiley, 2006.
- [7] S. Čorović et al., "The influence of skeletal muscle anisotropy on electroporation: In vivo study and numerical modeling," *Med. Biol. Eng. Comput.*, vol. 48, no. 7, pp. 637–648, Jul. 2010.
- [8] R. Šmerc et al., "A multiscale computational model of skeletal muscle electroporation validated using in situ porcine experiments," *IEEE Trans. Biomed. Eng.*, vol. 70, no. 6, pp. 1826–1837, Jun. 2023.
- [9] F. Xie and C. W. Zemlin, "Effect of twisted fiber anisotropy in cardiac tissue on ablation with pulsed electric fields," *PLoS One*, vol. 11, no. 4, Apr. 2016, Art. no. e0152262.
- [10] B. Kos et al., "Determination of lethal electric field threshold for pulsed field ablation in ex vivo perfused porcine and human hearts," Front. Cardiovasc. Med., vol. 10, Jun. 2023, Art. no. 1160231.
- [11] L. Molinari et al., "Multiscale and multiphysics modeling of anisotropic cardiac RFCA: Experimental-based model calibration via multi-point temperature measurements," Front. Physiol., vol. 13, Apr. 2022, Art. no. 845896.
- [12] M. Takaza et al., "The anisotropic mechanical behaviour of passive skeletal muscle tissue subjected to large tensile strain," *J. Mech. Behav. Biomed. Mater.*, vol. 17, pp. 209–220, Jan. 2013.
 [13] A. E. Knight et al., "Full characterization of in vivo muscle as an elastic,
- [13] A. E. Knight et al., "Full characterization of in vivo muscle as an elastic, incompressible, transversely isotropic material using ultrasonic rotational 3D shear wave elasticity imaging," *IEEE Trans. Med. Imag.*, vol. 41, no. 1, pp. 133–144, Jan. 2022.
- [14] D. Maji et al., "Enhancing in vivo Electroporation efficiency through hyaluronidase: Insights into plasmid distribution and optimization strategies," *Pharmaceutics*, vol. 16, no. 4, Apr. 2024, Art. no. 547.
- [15] M. Couade et al., "In vivo quantitative mapping of myocardial stiffening and transmural anisotropy during the cardiac cycle," *IEEE Trans. Med. Imag.*, vol. 30, no. 2, pp. 295–305, Feb. 2011.
- [16] A. Suzuki et al., "Impact of myocardial fiber orientation on lesions created by a novel heated saline-enhanced radiofrequency needle-tip catheter: An MRI lesion validation study," *Heart Rhythm*, vol. 18, no. 3, pp. 443–452, Mar. 2021.
- [17] V. Kovalev and F. Kruggel, "Texture anisotropy of the brain's white matter as revealed by anatomical MRI," *IEEE Trans. Med. Imag.*, vol. 26, no. 5, pp. 678–685, May 2007.
- [18] Y. Feng et al., "Measurements of mechanical anisotropy in brain tissue and implications for transversely isotropic material models of white matter," *J. Mech. Behav. Biomed. Mater.*, vol. 23, pp. 117–132, Jul. 2013.
- [19] R. W. Carlsen and N. P. Daphalapurkar, "The importance of structural anisotropy in computational models of traumatic brain injury," *Front. Neurol.*, vol. 6, Feb. 2015, Art. no. 28.
- [20] J. M. McMahon and D. J. Wells, "Electroporation for gene transfer to skeletal muscles: Current status," *BioDrugs*, vol. 18, no. 3, pp. 155–165, 2004.
- [21] J. De Vry et al., "In vivo electroporation of the central nervous system: A non-viral approach for targeted gene delivery," *Prog. Neurobiol.*, vol. 92, no. 3, pp. 227–244, Nov. 2010.
- [22] P. D. Fisher et al., "Adipose tissue: A new target for electroporationenhanced DNA vaccines," *Gene Ther.*, vol. 24, no. 12, pp. 757–767, Dec. 2017.
- [23] F. H. Wittkampf, R. Van Es, and K. Neven, "Electroporation and its relevance for cardiac catheter ablation," *JACC*, *Clin. Electrophysiol.*, vol. 4, no. 8, pp. 977–986, Aug. 2018.
- [24] E. Sokołowska and A. U. Błachnio-Zabielska, "A critical review of electroporation as a plasmid delivery system in mouse skeletal muscle," *IJMS*, vol. 20, no. 11, Jun. 2019, Art. no. 2776.
- [25] A. Sugrue et al., "Irreversible electroporation for catheter-based cardiac ablation: A systematic review of the preclinical experience," *J. Interv. Card Electrophysiol.*, vol. 55, no. 3, pp. 251–265, Sep. 2019.
- [26] A. Verma et al., "First-in-human experience and acute procedural outcomes using a novel pulsed field ablation system: The PULSED AF pilot trial," Circ, Arrhythmia Electrophysiol., vol. 15, no. 1, Jan. 2022, Art. no. e010168.
- [27] V. Y. Reddy et al., "Pulsed field or conventional thermal ablation for paroxysmal atrial fibrillation," *New England J. Med.*, vol. 389, no. 18, pp. 1660–1671, Nov. 2023.
- [28] A. Verma et al., "Pulsed field ablation for the treatment of atrial fibrillation: PULSED AF pivotal trial," *Circulation*, vol. 147, no. 19, pp. 1422–1432, May 2023.

- [29] K. -R. J. Chun et al., "State-of-the-art pulsed field ablation for cardiac arrhythmias: Ongoing evolution and future perspective," *Europace*, vol. 26, no. 6, Jun. 2024, Art. no. euae134.
- [30] L. M. Mir et al., "High-efficiency gene transfer into skeletal muscle mediated by electric pulses," *Proc. Nat. Acad. Sci. U. S. A.*, vol. 96, no. 8, pp. 4262–4267, Apr. 1999.
- [31] G. Tevz et al., "Gene electrotransfer into murine skeletal muscle: A systematic analysis of parameters for long-term gene expression," *Technol. Cancer Res. Treat.*, vol. 7, no. 2, pp. 91–101, Apr. 2008.
- [32] D. C. Hughes et al., "CORP: Gene delivery into murine skeletal muscle using in vivo electroporation," *J. Appl. Physiol.*, vol. 133, no. 1, pp. 41–59, Iul. 2022
- [33] T. Kotnik et al., "Membrane electroporation and electropermeabilization: Mechanisms and models," *Annu. Rev. Biophys.*, vol. 48, no. 1, pp. 63–91, May 2019.
- [34] T. Kotnik, G. Pucihar, and D. Miklavčič, "The cell in the electric field," in *Clinical Aspectsof*, S. T. Electroporation Kee, J. Gehl, and E. W. Lee, Eds. Berlin, Germany: Springer, 2011, pp. 19–29.
- [35] T. Polajzer, T. Jarm, and D. Miklavcic, "Analysis of damage-associated molecular pattern molecules due to electroporation of cells in vitro," *Radiol. Oncol.*, vol. 54, no. 3, pp. 317–328, Jul. 2020.
- [36] B. Geboers et al., "High-voltage electrical pulses in oncology: Irreversible electroporation, electrochemotherapy, gene electrotransfer, electrofusion, and electroimmunotherapy," *Radiology*, vol. 295, no. 2, pp. 254–272, May 2020.
- [37] S. Haberl et al., "Cell membrane electroporation-part 2: The applications," IEEE Electr. Insul. Mag., vol. 29, no. 1, pp. 29–37, Jan./Feb. 2013.
- [38] M. L. Yarmush et al., "Electroporation-based technologies for medicine: Principles, applications, and challenges," *Annu. Rev. Biomed. Eng.*, vol. 16, no. 1, pp. 295–320, Jul. 2014.
- [39] T. Kotnik et al., "Electroporation-based applications in biotechnology," *Trends Biotechnol.*, vol. 33, no. 8, pp. 480–488, Aug. 2015.
- [40] S. M. -Kalamiza, E. Vorobiev, and D. Miklavčič, "Electroporation in food processing and biorefinery," *J. Membrane Biol.*, vol. 247, no. 12, pp. 1279–1304, Dec. 2014.
- [41] G. Saldaña et al., "Microbiological aspects related to the feasibility of PEF technology for food pasteurization," *Crit. Rev. Food Sci. Nutr.*, vol. 54, no. 11, pp. 1415–1426, Nov. 2014.
- [42] S. Sachdev et al., "Revisiting the role of pulsed electric fields in overcoming the barriers to in vivo gene electrotransfer," *Bioelectrochemistry*, vol. 144, Apr. 2022, Art. no. 107994.
- [43] A. Cvetkoska et al., "Muscle contractions and pain sensation accompanying high-frequency electroporation pulses," *Sci. Reports*, vol. 12, no. 1, May 2022, Art. no. 8019.
- [44] V. Tayfur et al., "Anatomy of vastus lateralis muscle flap," J. Craniofacial Surg., vol. 21, no. 6, pp. 1951–1953, Nov. 2010.
- [45] S. D'Arpa et al., "Variability and reliability of the vastus lateralis muscle anatomy," Acta. Chirurgica. Belgica, vol. 116, no. 4, pp. 203–212, Jul. 2016.
- [46] S. Methenitis et al., "Intramuscular fibre conduction velocity and muscle fascicle length in human vastus lateralis," *Appl. Physiol. Nutr. Metab.*, vol. 44, no. 2, pp. 133–138, Feb. 2019.
- [47] E. C. de Almeida Araujo, "Adaptation of proof of concepts into quantitative NMR methods: Clinical application for the characterization of alterations observed in the skeletal muscle tissue in neuromuscular disorders," Ph.D. dissertation, Université Paris Sud Paris XI, Paris, France, 2014
- [48] A. Rehfeld, M. Nylander, and K. Karnov, Compendium of Histology: A Theoretical and Practical Guide. Berlin, Germany: Springer, 2017.
- [49] A. Sharifnezhad, R. Marzilger, and A. Arampatzis, "Effects of load magnitude, muscle length and velocity during eccentric chronic loading on the longitudinal growth of vastus lateralis muscle," J. Exp. Biol., Jan. 2014, Art. no. jeb.100370.
- [50] J. Feher, "Contractile Mechanisms in Skeletal Muscle," in *Quantitative Human Physiology*. New York, NY, USA: Elsevier, 2017, pp. 305–317.
- [51] J. Malmivuo and R. Plonsey, BioelectromagnetismPrinciples and Applications of Bioelectric and Biomagnetic Fields. London, U.K.: Oxford Univ. Press, 1995.
- [52] M. Kranjc et al., "Magnetic resonance electrical impedance tomography for monitoring electric field distribution during tissue electroporation," *IEEE Trans. Med. Imag.*, vol. 30, no. 10, pp. 1771–1778, Oct. 2011.
- [53] L. T. Muftuler et al., "In vivo MRI electrical impedance tomography (MREIT) of tumors," *Technol. Cancer Res. Treat.*, vol. 5, no. 4, pp. 381–387, Aug. 2006.

- [54] Y. Wang et al., "Mapping electrical properties heterogeneity of tumor using boundary informed electrical properties tomography (BIEPT) at 7 T," *Magn. Reson. Med*, vol. 81, no. 1, pp. 393–409, Jan. 2019.
- [55] H. J. Kim et al., "In vivo electrical conductivity imaging of a canine brain using a 3 t MREIT system," *Physiol. Meas.*, vol. 29, no. 10, pp. 1145–1155, Oct. 2008.
- [56] M. Åström, J. -J. Lemaire, and K. Wårdell, "Influence of heterogeneous and anisotropic tissue conductivity on electric field distribution in deep brain stimulation," *Med. Biol. Eng. Comput.*, vol. 50, no. 1, pp. 23–32, Jan. 2012.
- [57] G. Scott et al., "Sensitivity of magnetic-resonance current-density imaging," J. Magn. Reson., vol. 97, no. 2, pp. 235–254, Apr. 1992.
- [58] M. Joy, G. Scott, and M. Henkelman, "In vivo detection of applied electric currents by magnetic resonance imaging," *Magn. Reson. Imag.*, vol. 7, no. 1, pp. 89–94, Jan. 1989.
- [59] U. Mikac et al., "Magnetic resonance imaging of alternating electric currents," *Magn. Reson. Imag.*, vol. 19, no. 6, pp. 845–856, Jul. 2001.
- [60] G. C. Scott et al., "RF current density imaging in homogeneous media," Magn. Reson. Med, vol. 28, no. 2, pp. 186–201, Dec. 1992.
- [61] K. Beravs et al., "Electric current density imaging of bone by MRI," Magn. Reson. Imag., vol. 15, no. 8, pp. 909–915, Jan. 1997.
- [62] I. Serša et al., "Electric current density imaging of mice tumors," Magn. Reson. Med., vol. 37, no. 3, pp. 404–409, Mar. 1997.
- [63] R. S. Yoon et al., "Measurement of thoracic current flow in pigs for the study of defibrillation and cardioversion," *IEEE Trans. Biomed. Eng.*, vol. 50, no. 10, pp. 1167–1173, Oct. 2003.
- [64] E. Kossel and R. Kimmich, "Flow measurements below 50 Mm: NMR microscopy experiments in lithographic model pore spaces," *Magn. Reson. Imag.*, vol. 23, no. 2, pp. 397–400, Feb. 2005.
- [65] J. Pingel et al., "3D synchrotron imaging of muscle tissues at different atrophic stages in stroke and spinal cord injury: A proof-of-concept study," *Sci. Reports*, vol. 12, no. 1, Oct. 2022, Art. no. 17289.

- [66] T. Kotnik, D. Miklavčič, and T. Slivnik, "Time course of transmembrane voltage induced by time-varying electric fields—A method for theoretical analysis and its application," *Bioelectrochemistry Bioenergetics*, vol. 45, no. 1, pp. 3–16, Mar. 1998.
- [67] L. Rems et al., "Cell electrofusion using nanosecond electric pulses," Sci. Reports, vol. 3, no. 1, Nov. 2013, Art. no. 3382.
- [68] J. Dermol-Černe et al., "Plasma membrane depolarization and permeabilization due to electric pulses in cell lines of different excitability," *Bioelectrochemistry*, vol. 122, pp. 103–114, Aug. 2018.
- [69] I. Serša, M. Kranjc, and D. Miklavčič, "Current density imaging sequence for monitoring current distribution during delivery of electric pulses in irreversible electroporation," *BioMed. Eng. OnLine.*, vol. 14, no. S3, Dec. 2015, Art. no. S6.
- [70] I. Serša, "Auxiliary phase encoding in multi spin-echo sequences: Application to rapid current density imaging," *J. Magn. Reson.*, vol. 190, no. 1, pp. 86–94, Jan. 2008.
- [71] S. Huclova, D. Erni, and J. Fröhlich, "Modelling effective dielectric properties of materials containing diverse types of biological cells," *J. Phys. D, Appl. Phys.*, vol. 43, no. 36, Sep. 2010, Art. no. 365405.
- [72] S. Huclova, D. Erni, and J. Fröhlich, "Modelling and validation of dielectric properties of human skin in the MHz region focusing on skin layer morphology and material composition," *J. Phys. D, Appl. Phys.*, vol. 45, no. 2, Jan. 2012, Art. no. 025301.
- [73] J. D. -Černe and D. Miklavčič, "From cell to tissue properties—Modeling skin electroporation with pore and local transport region formation," *IEEE Trans. Biomed. Eng.*, vol. 65, no. 2, pp. 458–468, Feb. 2018.
- [74] M. Essone Mezeme et al., "Assessing how electroporation affects the effective conductivity tensor of biological tissues," *Appl. Phys. Lett.*, vol. 101, no. 21, Nov. 2012, Art. no. 213702.